

# Analysis of the Imaging Algorithms for Shape Detection and Shape Identification of a Target Using Through-the-Wall Imaging System

Akhilendra P. Singh<sup>1, \*</sup>, Smrity Dwivedi<sup>1</sup>, and Pradip K. Jain<sup>1, 2</sup>

**Abstract**—Through-the-Wall Imaging systems are a promising method for on-line applications, especially in disaster areas, where victims are buried under collapsed walls. These applications require such systems to identify the shape of the target. The foremost step while performing the task of shape recognition of stationary targets behind a wall is to first detect the target position, its approximate shape and size, and then, subsequent processing of these images with the use of signal processing techniques for the shape recognition of targets. For determining highly accurate information about target location and its approximate shape, a high-resolution image of the target is required. In literature, various imaging algorithms have been reported, some of which are back projection, delay sum, and frequency-wavenumber imaging algorithm. However, the use of these algorithms for shape detection of the target has not been explored so far. Therefore, it becomes essential to explore the use of these algorithms on TWI data to select an effective imaging algorithm for detecting approximate shape and size of the target. For this purpose, an experiment has been performed. The performances of these imaging algorithms have been analyzed and evaluated. The detected target images do not correspond to the actual shape and size of targets; therefore, a novel methodology using an artificial neural network has been presented for predicting the actual shape of the target. From the experimental data, the retrieved result of shape has been found in good agreement with the target original shape.

## 1. INTRODUCTION

Through wall radar imaging (TWRI) system is an emerging technology that is used to sense objects behind a wall using electromagnetic waves. This technology can be used for various applications such as military, law enforcement, and search and rescue missions [1]. These applications always require such systems to detect the target position, its approximate shape, and size, and subsequently identify the target behind walls. In previous articles, the use of time-frequency image or Doppler signatures for the identification of non-stationary targets has been reported. However, in the absence of frequency-domain or time-domain variation associated with a stationary target, these techniques become ineffective for the identification of stationary targets behind walls.

In previously reported article, identification of target in TWRI is achieved with the use of high range resolution profile (HRRP) based feature on segmented 3D dimensional through-the-wall images of the target [2]. As noted in their works, although the authors have obtained a good quality of results in the same orientation, but the proposed framework has not been modeled explicitly for orientation of the target. Thus, it will assign separate features for different orientations of the same target rather than having a single feature that covers all orientations. This will make the process complex and computationally intensive. A more promising technique for identifying the target is to estimate the shape of the target [3]. So, our main focus is laid on a shape identification of hidden objects, which is

---

*Received 21 September 2019, Accepted 19 November 2019, Scheduled 4 December 2019*

\* Corresponding author: Akhilendra Pratap Singh (apsingh.rs.ece14@itbhu.ac.in).

<sup>1</sup> Department of Electronics Engineering, Indian Institute of Technology (BHU), Varanasi, India. <sup>2</sup> Department of Electronics and Communication Engineering, National Institute of Technology, Patna, India.

also of great interest in many non-destructive applications especially in disaster areas, where victims are buried under collapsed walls, and small weapon detection through walls [4, 5]. Various authors have proposed a methodology for the shape estimation of the target behind a wall. In a previously reported article, the shape of the target has been estimated with the use of the Inverse Boundary Scattering Transform (IBST) on B-scan data [3] and the envelope of modified spheres on C-scan data [4]. With these algorithms, a quite accurate shape of the target has been achieved; however, these methods often need complex preprocessing like the IBST where wavefronts need to be recognized and estimated and the envelope of modified spheres where the curvature of target shape has to be estimated [6]. Recent development has achieved even higher accuracy but with a significant increase in complexity and computational time [6–8].

In the present article, a novel methodology for shape recognition of the target from TWRI images using wavelet descriptors and an artificial neural network is presented. This methodology is less complex and easy to implement. The proposed methodology can predict the shape of the target irrespective of its orientation and size. Instead of analyzing three-dimensional image of the target, we have analyzed a two-dimensional through-the-wall image of the target (horizontal cross-range vs vertical cross-range). The two-dimensional image of the target is extracted from a three-dimensional image of the target by selecting a plane at a fixed target range bin, which is selected by observing the range profile. The foremost step while performing the task of shape recognition of stationary targets behind a wall is to first detect the target position, its approximate shape and size, and then subsequent treatment of these images with the use of signal processing techniques for the shape recognition of targets. To determine highly accurate information about target location and its approximate shape, a high-resolution image of the target is required. Thus, one of the significant challenges in TWI is to develop an efficient imaging algorithm that can give maximum information about target [1]. In previous articles, various imaging algorithms have been reported in the literature. So, it becomes essential to explore the use of these algorithms with through-wall imaging (TWI) data to analyze the effect of imaging and evaluating the performance [9]. The most commonly used technique in TWI for image formations is back projection (BP) [10], delay and sum beamforming (DS) [11], and frequency-wavenumber (F-K) [12]. So far, very little work has been reported for the application of these three imaging techniques on the same data and checking the consequences and effects of imaging. Therefore, the main focus of this paper is to first see the possibility of these imaging techniques on real data and compare their results to select the effective imaging algorithm. The through-the-wall radar images show very little resemblance to optical images due to which it becomes difficult to interpret from the imaged scene. Therefore, this through-the-wall image of the target is further processed using the artificial neural network (ANN) for determining the actual shape of the target. An effective training technique is used to improve the effectiveness of the proposed algorithm. The paper is organized as follows. Section 2 describes different imaging techniques commonly used in TWI and experimental setup and measurement procedures used in TWI. Section 3 describes the shape recognition model and results obtained from it, which is followed by conclusions in Section 4.

## 2. ANALYSIS OF IMAGING ALGORITHM

Imaging algorithms play an essential role in determining the approximate shape and size of the target for which numerous imaging algorithms have been reported. In the present article, back projection, delay and sum beamforming, and frequency-wavenumber imaging algorithms have been considered for the formation of high-resolution images. Backprojection imaging algorithm is a traditional range migration or time-domain algorithm and has been widely used for focusing in through wall imaging (TWI) and ground penetrating radar (GPR) application [10, 13, 14]. In this method, the data received at each scan point using the SFCW system are Inverse Fourier Transformed to produce a range domain before forming the image. This method correlates the spatial position of scan point and pixels of the desired image map to the range profile. The idea is to correlate data collected at each scan point position as a function of round-trip delay. It coherently sums the sampled radar returns for each scan point position. The delay and sum imaging algorithm derived from the beamforming algorithm is a traditional frequency-domain algorithm and is also widely used for focusing in TWI systems [11]. For cases where the frequency steps are not even, images are formed by delay and sum imaging algorithm [10]. In this method, for each pixel

in the image, the frequency data are phase adjusted one frequency at a time. Frequency-wavenumber imaging technique is also a traditional frequency-domain algorithm and has been used for focusing in TWI and GPR [12–14]. This gives a less computation time with respect to the back projection and delay sum imaging algorithms. Brief discussions about the implementation of these imaging algorithms are as follows.

## 2.1. Back Projection

For the monostatic stepped frequency continuous wave (SFCW) radar system, the received signal measured at scan point position  $x, y$  scattered from  $P$  point targets at the position  $x_{p_i}, y_{p_i}, z_{p_i}$  can be given as [10]

$$S(x, y, f_k) = \sum_{i=1}^P a(x_{p_i}, y_{p_i}, z_{p_i}) \exp(-\alpha(j2\pi f_k \tau_{p_i})) \quad (1)$$

where  $f_k$  is the frequency point;  $\tau_{p_i}$  is the propagation delay from the scan point at position  $x, y$  to the pixel at position  $x_{p_i}, y_{p_i}, z_{p_i}$  and then back to the same scan point;  $a(x_{p_i}, y_{p_i}, z_{p_i})$  is the target reflectivity;  $\alpha$  is the attenuation constant of wall. Backprojection is an image reconstruction technique applied on range profile data. In order to implement backprojection algorithm on SFCW TWI data, Inverse Fourier Transform has been carried out on TWI data measured at each scan point. The data received  $S(x, y, f_k)$  in frequency-domain for each scan point at position  $x, y$  is Inverse Fourier Transformed to produce received TWI data in the range domain  $S(x, y, z)$  using Eq. (2) as proposed in [15].

$$S(x, y, z) = \sum_{k=1}^L S(x, y, f_k) \exp(j2\pi f_k(2z/c)) \quad (2)$$

where  $L$  is number of frequency points, and  $R_{p_i}$  is the distance traveled from scan point at position  $x, y$  to target point at the position  $x_{p_i}, y_{p_i}, z_{p_i}$ . For each pixel in the desired image map, the propagation range  $R_{p_i}$ , i.e., the distance traveled from the scan point at position  $x, y$  to the pixel at the position  $x_{p_i}, y_{p_i}, z_{p_i}$  and then back to the same scan point, is calculated using Eq. (3) as proposed in [11]

$$R_{p_i} = 2l_{airtowell} + 2\sqrt{\epsilon}l_{wall} + 2l_{walltoair} \quad (3)$$

The variables  $l_{airtowell}$ ,  $l_{wall}$ ,  $l_{walltoair}$  represent the distance traveled by a signal before, through, and beyond the wall from scan point at position  $x, y$  to the pixel in desired image map at position  $x_{p_i}, y_{p_i}, z_{p_i}$ . The details of the calculation of the propagation range are described in [11].

The propagation range is further used to select the range cell in the range profile to get the value of the in-phase and quadrature components of the scattered field for that range cell for all the scan points. The values of the in-phase and quadrature components for all the scan points are summed for each pixel in the image map. Thus, the value of a pixel  $I(x_{p_i}, y_{p_i}, z_{p_i})$  at the position  $x_{p_i}, y_{p_i}, z_{p_i}$  corresponding to a point scatter at the position  $x_{p_i}, y_{p_i}, z_{p_i}$  can be given by using Eq. (4) as proposed by [15]

$$I(x_{p_i}, y_{p_i}, z_{p_i}) = \sum_{x=1}^M \sum_{y=1}^N S(x, y, z = R_{p_i}) \quad (4)$$

The above backprojection imaging algorithm can be implemented in the following steps:

- i. The C-scan data representing back-scattered electric field  $S(x, y, f_k)$  in the frequency domain is collected.
- ii. The data received at each scan point are inverse Fourier transformed to produce a range profile  $S(x, y, z)$ .
- iii. The whole image map is divided into small pixels.
- iv. The propagation range is calculated from one scan point to the pixel position and then back to the same scan point for each pixel in the desired image-map.
- v. The propagation range calculated is further used to select the range bin in the range profile.
- vi. The Corresponding received range bin amplitude value of scattered field is recorded.

- vii. The above step is repeated for all scan points.
- viii. The values of the recorded amplitude value from all scan points are added for each pixel in image map.

## 2.2. Delay and Sum Beamforming

The delay and sum beamforming is a frequency-domain image reconstruction technique [11]. For the monostatic SFCW radar system, the received signal measured  $S(x, y, f_k)$  at scan point position  $x, y$  scattered from  $P$  point targets at positions  $x_{p_i}, y_{p_i}, z_{p_i}$  can be given as [10]

$$S(x, y, f_k) = \sum_{i=1}^P a(x_{p_i}, y_{p_i}, z_{p_i}) \exp(-\alpha(j2\pi f \tau_{p_i})) \quad (5)$$

For each pixel in the desired image map, the propagation delay from one scan point at position  $x, y$  to the pixel at the position  $x_{p_i}, y_{p_i}, z_{p_i}$  and then back to the same scan point is calculated using Eq. (6) as proposed by [11]

$$\tau_{p_i} = \frac{2l_{airtowall}}{c} + \frac{2l_{wall}}{v} + \frac{2l_{walltoair}}{c} \quad (6)$$

Here  $c$  is the velocity of signal propagation in air, and  $v$  is the velocity of signal propagation through the wall. The variables  $l_{airtowall}$ ,  $l_{wall}$ ,  $l_{walltoair}$  represent the distance travelled by a signal before, through, and beyond the wall from scan point at position  $x, y$  to the pixel in desired image map at position  $x_{p_i}, y_{p_i}, z_{p_i}$ . The detailed calculation of propagation delay can be found in [11].

The value of each pixel  $I(x_{p_i}, y_{p_i}, z_{p_i})$  at position  $x_{p_i}, y_{p_i}, z_{p_i}$  is estimated after applying phase delays  $\exp(j2\pi f_k \tau_{p_i})$  to outputs of the C-scan data in frequency-domain  $S(x, y, f_k)$  to synchronize the signal arrived at all scan points and then summing the delayed signals using Eq. (7) as proposed in [11]

$$I(x_{p_i}, y_{p_i}, z_{p_i}) = \sum_{x=1}^M \sum_{y=1}^N \sum_{k=1}^L S(x, y, f_k) \exp(j2\pi f_k \tau_{p_i}) \quad (7)$$

where  $L$  represents the number of frequency points.

The above delay and sum beamforming imaging algorithm can be implemented in the following steps:

- i. The C-scan data representing back-scattered electric field  $S(x, y, f_k)$  in the frequency domain are collected. Divide the whole image map into small pixels.
- ii. The propagation delay is calculated from one scan point to the pixel position and then back to the same scan point for each pixel in the desired image-map.
- iii. The propagation delay has been applied to the data collected at each antenna location for all frequency points.
- iv. The received data for all the frequency points are added.
- v. The above step is repeated for all scan points.
- vi. The results obtained for all scan points are summed to form the image.

## 2.3. Frequency-Wave Number

For the monostatic SFCW radar system, the received signal measured at scan point scattered from a single point target can be given in terms of wavenumber as [13, 14]

$$S(x, y, f) = \rho \cdot \exp(-j2kd) \quad (8)$$

where  $k = 2\pi f/\nu$  is the wavenumber vector, and  $\rho$  is the strength of the field scattered from the point target. The received field from  $P$  point targets located at different  $(x_i, y_i, z_i)$  positions assuming homogeneous wall can be given as [13, 14]

$$S(x, y, f) = \sum_{i=1}^P \rho_i \cdot \exp(-jk(2\sqrt{z_i^2 + (x-x_i)^2 + (y-y_i)^2})) \quad (9)$$

Applying two-dimensional 2D Fourier transform to  $S(x, y, f)$  along the  $x$ -direction and  $y$ -direction, the frequency-wavenumber domain of scattered data can be represented as [12]

$$S(k_x, k_y, f) = \sum_{i=1}^P \rho_i \cdot \int_{-\infty}^{\infty} \int_{-\infty}^{\infty} \left( \exp(-jk(2\sqrt{z_i^2 + (x-x_i)^2 + (y-y_i)^2})) \right) \cdot \exp(jk_x x) dx \exp(jk_y y) dy \quad (10)$$

This is the received signal data in  $k_x k_y - f$  domain. It can be assumed that a total of  $P$  point targets are ideally imaged in real coordinates as

$$S(x, y, z) = \sum_{i=1}^P \rho_i \cdot \delta(x - x_{p_i}, y - y_{p_i}, z - z_{p_i}) \quad (11)$$

where  $\delta(x, y, z)$  is the two-dimensional impulse function. After applying the three-dimensional Fourier transform to this ideal image data with respect to  $x, y$ , and  $z$ , the following scattered field value  $\bar{S}(k_x, k_y, k_z)$  in the spatial-frequency domain is obtained which is given as

$$\bar{S}(k_x, k_y, k_z) = \sum_{i=1}^P \rho_i \cdot \exp(-jk_x x_{p_i} - jk_y y_{p_i} - jk_z z_{p_i}) \quad (12)$$

Then, mapping of  $S(k_x, k_y, f)$  data is done from  $k_x k_y - f$  domain to  $k_x k_y k_z$  domain by using interpolation to obtain  $\bar{S}(k_x, k_y, k_z)$  by relating the values of  $S(k_x, k_y, f)$  at each  $f$  point to the values of  $\bar{S}(k_x, k_y, k_z)$  at  $k_z$  points with the help of the frequency mapping equation  $k_z = \sqrt{4k^2 - k_x^2 - k_y^2}$ . Afterward, the final focused image spotting the true locations of the point target is obtained by taking the three-dimensional IFFT of Eq. (10) as [12, 13]

$$I(x_{p_i}, y_{p_i}, z_{p_i}) = \frac{1}{(2\pi)^3} \int_{-\infty}^{\infty} \int_{-\infty}^{\infty} \int_{-\infty}^{\infty} \bar{S}(k_x, k_y, k_z) \exp(jk_x \cdot x + jk_y \cdot y + jk_z \cdot z) dk_x dk_y dk_z \quad (13)$$

Here,  $I(x_{p_i}, y_{p_i}, z_{p_i})$  represents the value of a pixel at the position  $x_{p_i}, y_{p_i}, z_{p_i}$  in the image domain.

The above frequency-wavenumber imaging algorithm can be implemented in the following steps:

- i. The C-scan data representing back-scattered electric field  $S(x, y, f)$  in the frequency domain is collected. Divide the whole image map into small pixels.
- ii. A two-dimensional Fourier transform is applied on  $S(x, y, f)$  along synthetic aperture  $x$  and  $y$  to get  $S(k_x, k_y, f)$  and normalizes it.
- iii.  $S(x, y, f)$  is interpolated on to a rectangular mesh in  $k_x k_y k_z$  domain to obtain  $\bar{S}(k_x, k_y, k_z)$ .
- iv. A three-dimensional IFFT  $\bar{S}(k_x, k_y, k_z)$  is taken to form the final focused three-dimension image  $I(x_{p_i}, y_{p_i}, z_{p_i})$  in Cartesian coordinates.

#### 2.4. Performance of Imaging Algorithms

To analyze the effect of imaging algorithms on real data, an experiment is carried out with the help of a monostatic (SFCW) radar system. Figure 1 shows a schematic representation of the monostatic SFCW radar system. The system consists of an Anritsu VNA MS2037C and horn, which works in the frequency range of 3.5–5.5 GHz. Table 1 shows typical values of designed SFCW radar parameters considered for imaging.

The antenna is placed on a 2D moving platform for movement in horizontal direction and vertical direction. The radar is kept at 220 cm from the wall. The target is kept at 122 cm on the other side of the wall. The target is placed on a wooden stand which is covered with an absorbing sheet to minimize any reflection from the stand. Four targets with different shapes and sizes, T1, T2, T3, and T4, have been considered. The details of the targets are given in Table 2. In order to acquire entire information of scene behind walls,  $S$ -parameter  $S_{11}$  is collected at 21 horizontal and 21 vertical scan points to cover the target completely. The inter-element spacing between scan points is 5 cm.

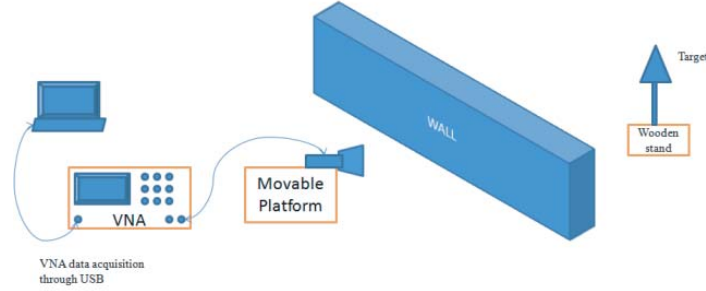


**Figure 1.** Schematic diagram for through-the-wall radar imaging system [15].

**Table 1.** Typical values of SFCW radar parameters.

Radar parameters	Value
Frequency range	3.5 GHz–5.5 GHz
Bandwidth	2 GHz
Number of frequency points	201
Power Transmitted	–3 dBm
Down Range Resolution	7.5 cm
Cross-range Resolution	11.06 cm
Antenna Type	Horn
Beam Width	20 degree
Gain	18 dB

**Table 2.** List of target samples used in experiment.

Target ID	Shape	Size (Length × Width)	Orientation	Material
T1	Circle	Dia = 30 cm	0	Metal
T2	Circle	Dia = 35 cm	0	Metal
T3	Square	30 cm × 30 cm	0	Metal
T4	Rectangle	50 cm × 30 cm	0	Metal

Before forming the 2D TWRI image of the target, it is essential to know the characteristics of the wall (i.e., dielectric constant), presence of the target, and its location. These things affect the quality of the image. Estimation of wall dielectric is done in a similar manner as proposed by Muqaible and Safaai-Jazi [16]. The dielectric value of the wall is found to be 6.4. For finding target location, the range profile at one of the scan points from the measured C-scan data using measurement setup is analyzed. The range profile can be represented as [15]

$$S(z) = \sum_{m=1}^{201} S(f_k) \exp(j2\pi f_k(2z/c + R_{delay} + 2d_{wall}(\sqrt{\varepsilon_{wall}} - 1)/c)) \quad (14)$$

where  $R_{delay}$  is the delay due to antenna system,  $d_{wall}$  the wall thickness,  $\varepsilon_{wall}$  the wall dielectric, and  $f_k$  the frequency. To estimate the delay due to the antenna system, a separate experiment has been carried out similarly as described in [15]. Figure 2 shows the range profile plot for one of the scan points

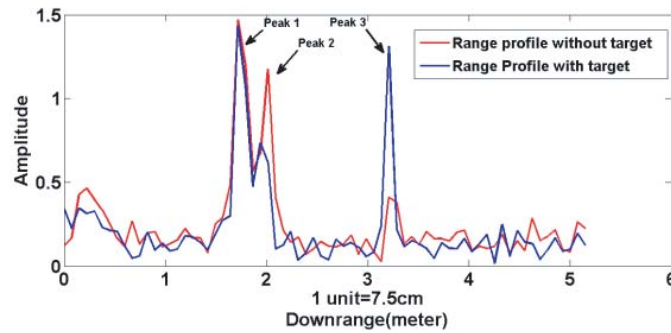


**Figure 2.** Range profile plot.

of the C-scan data at which target reflections occurs. In the shown range profile plot, the first two peaks are due to reflections from the front and rear sides of the wall, and the third peak shows reflection from the target. Thus, the target downrange location has been calculated from the range profile.

Once the wall parameter and target downrange position are estimated, the acquired C-scan data are further processed for the formation of 2D through-the-wall radar images using back projection, frequency wavenumber, and delay and sum beamforming. The two-dimensional image of the target (height vs cross-range) is plotted by considering a  $Y$  plane at a fixed target range bin ( $z = z_{target}$ ) which is selected by observing range profile. Thus, a virtual imaging plane of size  $50 \times 50$  is created.

Different imaging algorithms have been applied on acquired TWI data with various shapes of considered targets T1, T2, T3, and T4 to analyze the effect of the imaging. The 2D TWRI image of considered targets using each imaging algorithm is shown in Figures 3(a)–(l). In Figures 3(a)–(l),  $X$ -axes represent cross-range, and  $Y$ -axes represent the height of the target.

The shape of the target has been extracted after applying thresholding on the 2D TWRI using the statistical method [17]. The threshold value is calculated as

$$Th = mean + standard\ deviation \quad (15)$$

The thresholded 2D TWRI shape of considered targets using each imaging algorithm is shown in Figures 4(a)–(p) along with the reference shape of the target. The number of target pixels of reference target shape has been obtained based on a priori information of target size, location, and size of pixel [18–20]. As per experimental results with various target samples, a considerable difference between the output images of algorithms from the focusing point of view is observed. From Figures 4(a)–(p), it is observed that though the considered imaging algorithm has accurately detected the position of the target, BP and F-K algorithms perform poorly in detecting approximate size and shape of the target. The shape and size of the target detected are compared with the reference target shape. The comparison between the number of target pixels detected using each imaging algorithm and the number of target pixels in reference target shape is shown in Table 3. From Table 3, it is observed that with the delay sum imaging technique, the numbers of target pixels detected are close to the number of target pixels of reference target shape as compared to frequency-wavenumber and backprojection imaging technique. This shows that delay and sum imaging algorithm proves to be a more effective imaging tool than backprojection and frequency-wavenumber imaging algorithms for detecting approximate shape and size of the target.

Moreover, we have analyzed the useful information about the statistics of the target image formed with considered imaging algorithms. Using the thresholded binary image, the raw 2D TWRI image is masked, producing 2D TWRI image with the target region only. The statistics of the target image are obtained using commercially available, easy fit software [21]. Various probability density functions (pdf), available in easy fit software, are analyzed for evaluating the probability density function of the target image. For evaluating the probability density function target image, a Kolmogorov-Smirnov (KS) goodness of fit test is performed on various probability density functions. Only those pdf functions have been selected, which have passed the KS test on the basis that statistic value should be less than critical value and that p-value is greater than the level of significance (5%). The probability density functions of the target image are evaluated for considered targets of different shapes for each imaging algorithm.

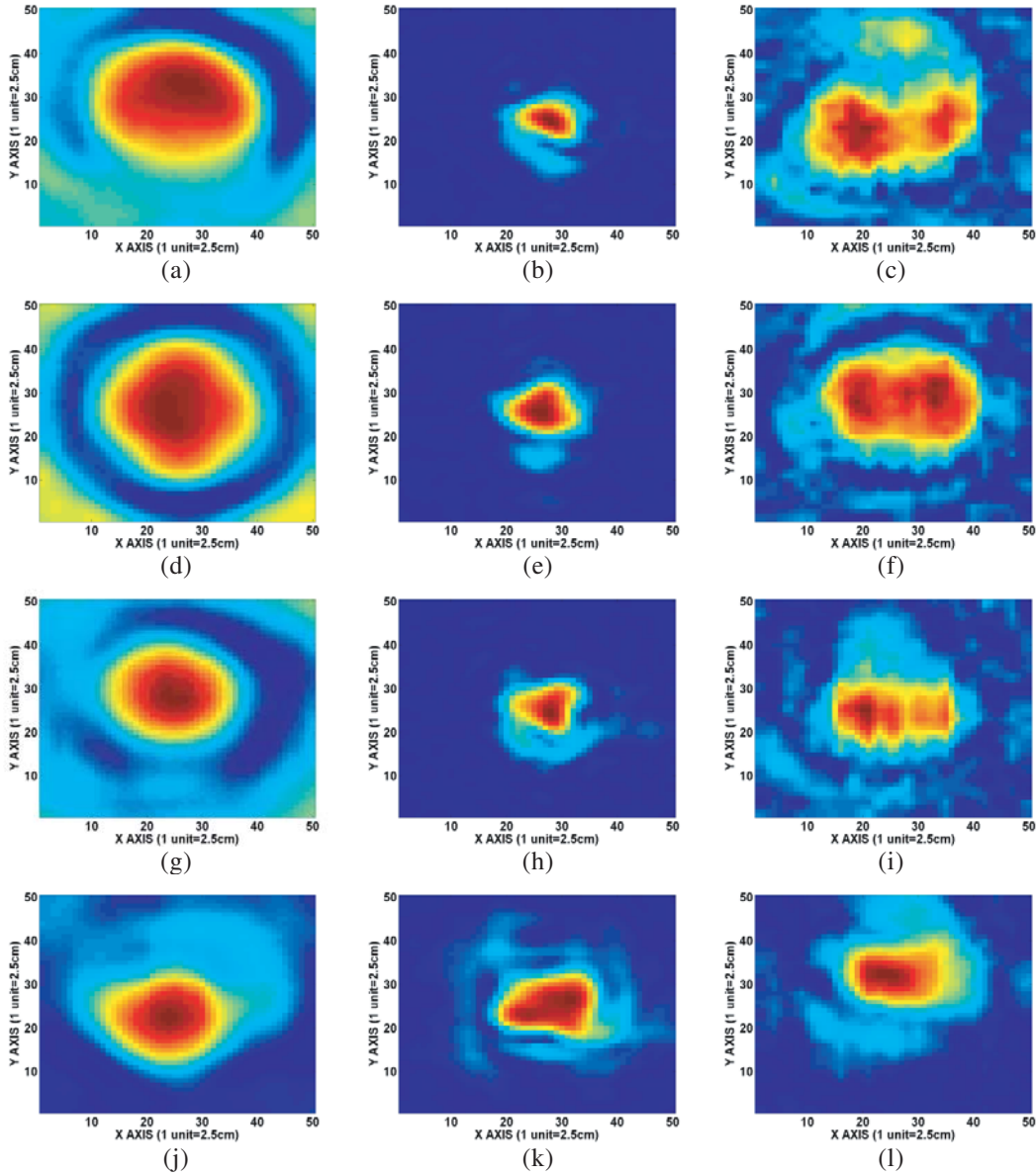


**Figure 3.** (a) Raw 2D TWRI Image obtained using backprojectionimaging method on imaging plane along  $X$  and  $Y$  axis of target id T1. (b) Raw 2D TWRI Image obtained using delay and sum imaging method on imaging plane along  $X$  and  $Y$  axis of target id T1. (c) Raw 2D TWRI Image obtained using frequency wave number imaging method on imaging plane along  $X$  and  $Y$  axis of target id T1. (d) Raw 2D TWRI Image obtained using back projection imaging method on imaging plane along  $X$  and  $Y$  axis of target id T2. (e) Raw 2D TWRI Image obtained using delay and sum imaging method on imaging plane along  $X$  and  $Y$  axis of target id T2. (f) Raw 2D TWRI Image obtained using frequency wave number imaging number method on imaging plane along  $X$  and  $Y$  axis of target id T2. (g) Raw 2D TWRI Image obtained using backprojectionimaging method on imaging plane along  $X$  and  $Y$  axis of target id T3. (h) Raw 2D TWRI Image obtained using delay and sum imaging method on imaging plane along  $X$  and  $Y$  axis of target id T3. (i) Raw 2D TWRI Image obtained using frequency wave number imaging method on imaging plane along  $X$  and  $Y$  axis of target id T3. (j) Raw 2D TWRI Image obtained using back projection imaging method on imaging plane along  $X$  and  $Y$  axis of target id T4. (k) Raw 2D TWRI Image obtained using delay and sumimaging method on imaging plane along  $X$  and  $Y$  axis of target id T4. (l) Raw 2D TWRI Image obtained using frequency-wavenumber imaging method on imaging plane along  $X$ -axis and  $Y$ -axis of target id T4.

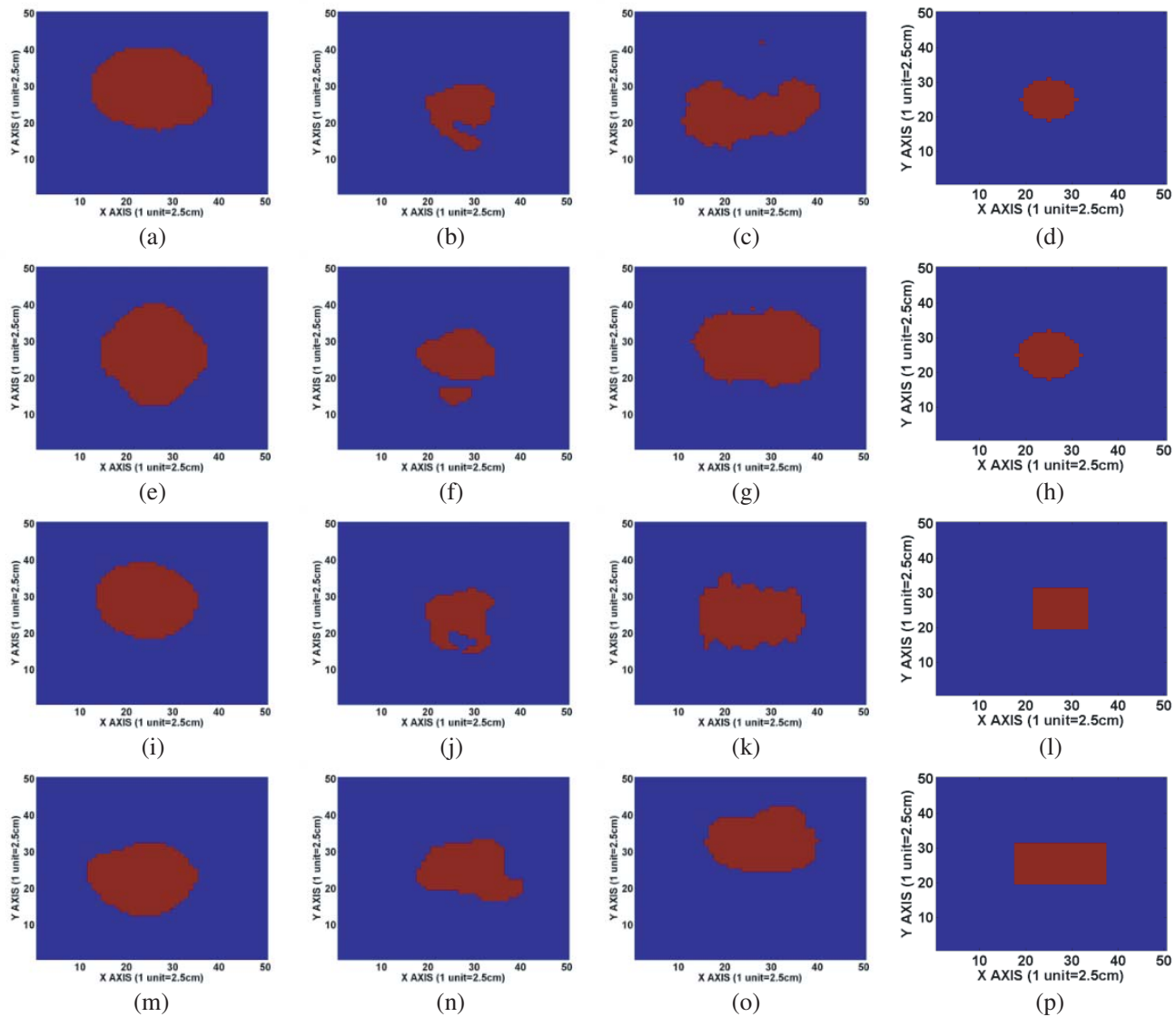


**Figure 4.** (a) Raw 2D TWRI Image obtained using backprojection imaging method on imaging plane along  $X$  and  $Y$  axis of target id T1. (b) Raw 2D TWRI Image obtained using delay and sum imaging method on imaging plane along  $X$  and  $Y$  axis of target id T1. (c) Raw 2D TWRI Image obtained using frequency-wave number imaging method on imaging plane along  $X$  and  $Y$  axis of target id T1. (d) Reference target shape of target id T1. (e) Raw 2D TWRI Image obtained using backprojection imaging method on imaging plane along  $X$  and  $Y$  axis of target id T2. (f) Raw 2D TWRI Image obtained using delay and sum imaging method on imaging plane along  $X$  and  $Y$  axis of target id T2. (g) Raw 2D TWRI Image obtained using frequency-wavenumber imaging method on imaging plane along  $X$  and  $Y$  axis of target id T2. (h) Reference target shape of target id T2. (i) Raw 2D TWRI Image obtained using back projection imaging method on imaging plane along  $X$  and  $Y$  axis of target id T3. (j) Raw 2D TWRI Image obtained using delay and sum imaging method on imaging plane along  $X$  and  $Y$  axis of target id T3. (k) Raw 2D TWRI Image obtained using frequency-wavenumber imaging method on imaging plane along  $X$  and  $Y$  axis of target id T3. (l) Reference target shape of target id T3. (m) Raw 2D TWRI Image obtained using backprojection imaging method on imaging plane along  $X$  and  $Y$  axis of target id T4. (n) Raw 2D TWRI Image obtained using delay and sum imaging method on imaging plane along  $X$  and  $Y$  axis of target id T4. (o) Raw 2D TWRI Image obtained using frequency wavenumber imaging method on imaging plane along  $X$  and  $Y$  axis of target id T4. (p) Reference target shape of target id T4.

**Table 3.** No. of target pixels detected in 2D TWRI of the considered target using different imaging algorithm.

Targets	No. of targets pixels detected In Backprojection image	No. of target pixels detected In Delay Sum image	No. of target pixels detected In Frequency-Wavenumber image	No. of target pixels in reference target shape
T1	470	173	381	144
T2	470	210	466	196
T3	362	184	351	144
T4	362	272	342	240

**Table 4.** KS statistics and fitting parameter for distributions of target image in 2D TWRI for target Id T1, T2, T3, and T4 for different imaging algorithm.

Imaging Algorithms	Pdf	Statistics	Target T1	Target T2	Target T3	Target T4
Back-projection	Beta	Statistics	0.02683	0.0176	0.01701	0.01944
		P-value	0.87848	0.99815	0.9999	0.99881
		Critical value	0.06264	0.06264	0.07137	0.07137
		Fitting Parameters	$\alpha_1 = 1.1474$ $\alpha_2 = 1.0165$ $a = 0.68875$ $b = 1.0$	$\alpha_1 = 0.96525$ $\alpha_2 = 0.81424$ $a = 0.68231$ $b = 1.0$	$\alpha_1 = 0.94697$ $\alpha_2 = 0.99075$ $a = 0.54975$ $b = 1.0$	$\alpha_1 = 0.90775$ $\alpha_2 = 1.0182$ $a = 0.51176$ $b = 1.0$
Delay and Sum	Beta	Statistics	0.07459	0.05245	0.04368	0.05667
		P-value	0.27683	0.59145	0.85869	0.33415
		Critical value	0.10325	0.09371	0.10011	0.08234
		Fitting Parameters	$\alpha_1 = 0.55899$ $\alpha_2 = 1.1222$ $a = 0.27584$ $b = 1.0125$	$\alpha_1 = 0.62207$ $\alpha_2 = 0.87022$ $a = 0.26461$ $b = 1.0$	$\alpha_1 = 0.61138$ $\alpha_2 = 1.0845$ $a = 0.3427$ $b = 1.0$	$\alpha_1 = 0.75844$ $\alpha_2 = 0.739$ $a = 0.39348$ $b = 1.0$
Frequency-wavenumber	Weibull	Statistics	0.04569	0.05318	0.06759	0.0698
		P-value	0.39223	0.13821	0.07726	0.06803
		Critical value	0.06957	0.06291	0.07248	0.07343
		Fitting Parameters	$\alpha = 1.6266$ $\beta = 0.17504$ $\gamma = 0.60852$	$\alpha = 3.7796$ $\beta = 0.38852$ $\gamma = 0.43273$	$\alpha = 1.9381$ $\beta = 0.28158$ $\gamma = 0.41659$	$\alpha = 1.287$ $\beta = 0.24285$ $\gamma = 0.42861$

The pdf of the target image of the considered target for each imaging algorithm is shown in Table 4. From Table 4, it is observed that the probability distribution of the target images changes with imaging algorithm. For example, backprojection and beamforming have Beta distribution, whereas frequency-wavenumber has Weibull distribution. The probability density function of Weibull and Beta is given by [22]

$$f(x) = \frac{\alpha}{\beta} \left( \frac{x-y}{\beta} \right)^{\alpha-1} \exp\left(-\frac{x-y}{\beta}\right)^{\alpha} \quad (16)$$

where  $\alpha, \beta$  are shape parameters, and  $\gamma$  is the continuous location parameter.

$$f(x) = \frac{1}{B(\alpha_1, \alpha_2)} \frac{(x-a)^{\alpha_1-1} (b-x)^{\alpha_2-1}}{(b-a)^{\alpha_1+\alpha_2-1}} \tag{17}$$

where  $\alpha_1$  and  $\alpha_2$  are shape parameters, and  $a$  and  $b$  are continuous boundary parameters.

It is also observed that the pdf of the target image with delay sum imaging algorithm, back projection, and frequency-wavenumber imaging technique appears to consistently follow a single probability density function for different considered targets. This shows that a single probability density based function captures the true properties of the backscattered signal. However, the shape parameter of weibull distribution changes with the small change in target geometry, and shape parameter of beta distribution remains almost constant with change in target geometry. This shows that a small change in target geometry provides a large change in the probability distribution of target image with a frequency-wavenumber algorithm, hence the possibility of the false alarms rate while performing detection of the target will be higher with frequency-wavenumber imaging algorithm and lower with backprojection and beamforming imaging technique.

Further, to analyze quality of 2D through-the-wall radar image of the target with these imaging algorithms, Peak to Signal Noise ratio (PSNR) is computed. PSNR is computed using Eqs. (14), (15) as

$$MSE = \frac{1}{MXN} \sum_{i=1}^N \sum_{j=1}^M (F(i, j) - I(i, j))^2 \tag{18}$$

$$PSNR(\text{dB}) = 10 \log \left( \frac{1}{MSE} \right) \tag{19}$$

where  $I$  represents a 2D TWRI image without a target;  $F$  represents a raw 2D TWRI image with the target;  $M$  represents the number of pixels in row; and  $N$  represents the number of pixels in columns. The image quality of different algorithms can be visibly observed from the obtained results. From Table 5, it is observed that peak to signal noise of formed images using delay and sum beamforming imaging technique is high and closely followed by backprojection and frequency-wavenumber imaging algorithm. A high PSNR shows that a good contrast is present between the pixels corresponding to the target and background pixels. Thus, the shape of the target can be easily detected.

**Table 5.** PSNR (dB) value of imaging algorithm for target id T1, T2, T3, T4.

Targets	Backprojection	Delay and Sum	Frequency-wavenumber
T1	9.3175	11.7132	10.9223
T2	9.2833	11.4005	10.5186
T3	11.2491	11.8652	12.1104
T4	11.4193	11.7823	11.7669

In the present paper, our main aim is to select an efficient image reconstruction algorithm that can give maximum information about targets such as its location, approximate shape, and size. For this purpose, we have analyzed the effect of delay and sum beamforming, backprojection, and frequency-wavenumber imaging algorithms image reconstruction on approximate shape and size of the target, peak to signal noise ratio of image, and probability distribution of target image with different shapes and sizes of TWI data. For detecting target pixels with a low false alarm, the probability distribution of target image should not change with target geometry, and the contrast of image should be high. From the experimental results, it is observed that peak to signal noise of formed images using delay sum imaging technique is high and closely followed by backprojection and frequency-wavenumber imaging algorithm which shows that a high-quality 2D TWI images of the target can be obtained with delay and sum beamforming algorithm, backprojection, and frequency-wavenumber imaging algorithm. It is also

observed that the probability distribution of the target images changes with the imaging algorithm. For example, backprojection and beamforming have Beta distribution, whereas frequency-wavenumber has Weibull distribution. Moreover, a small change in target geometry provides a large change in the shape parameters of Weibull distribution whereas shape parameters of Beta distribution do not change much with small change target geometry. It shows that the probability distribution of frequency-wavenumber image of target changes as target geometry changes, hence possibility of the false alarms rate will be higher with frequency-wavenumber imaging algorithm. Thus, delay and sum beamforming and backprojection algorithm are useful for detecting the location of a target with a low false alarm. However, backprojection and frequency-wavenumber imaging algorithms have poorly reconstructed approximate shape and size of the target compared to the delay and sum beamforming imaging algorithm. It has been observed that with delay and sum beamforming imaging technique, numbers of target pixels detected are close to the number of target pixels of reference target shape in comparison with frequency-wavenumber and backprojection imaging technique. Thus, delay and sum, and backprojection imaging algorithms can be used to detect the target with a low false alarm, but for detecting approximate shape and size of the target, delay and sum imaging algorithm proves to be a more effective imaging tool than backprojection and frequency-wavenumber imaging algorithms.

### 3. DEVELOPMENT OF MODEL FOR SHAPE IDENTIFICATION OF TARGET

From the previous discussion, it has been observed that BP and F-K imaging techniques perform poorly in determining approximate shapes and sizes of the target as compared to delay and sum beamforming imaging techniques. Therefore, delay and sum beamforming imaging has been considered for the development of a target shape recognition model. The detected target images do not correspond to the actual shape and size of targets; therefore, there is a need for a methodology for the analysis of radar images, which can automatically perform recognition tasks and thereby help in decision making. Therefore, this 2D TWRI of the target using delay and sum beamforming imaging algorithm is further processed using an artificial neural network (ANN) to determine the actual shape of the target. The image formed has  $50 \times 50$  pixels, which is a low-resolution image. The image resolution is increased by interpolation. Shape-preserving interpolation is used [17]. To identify the shape of the target, a feature that gives a description of target is required. The feature is extracted by applying 1D Wavelet Transform on the boundary of target. Shape identification of target can be achieved by comparing and matching the descriptors of the retrieved target image with descriptors of the synthetic image. One of the major problems which occurs in recognizing the shape of the targets is with its orientation. It is difficult to identify the particular shape of the target with a slight orientation effect. Thus, in order to make model orientation and scale-invariant, an orientation and scale-invariant feature is required. The feature is obtained by applying one-dimensional discrete wavelet transform (1D DWT) on the boundary of each shape. Using the 4-level Daubechies 1D DWT, the boundary of each shape described as  $(x_i; y_i)$  is decomposed into approximated residual signals and detailed signals. This representation is presented as

$$\begin{bmatrix} x(m) \\ y(m) \end{bmatrix} = \begin{bmatrix} x_a(m) \\ y_a(m) \end{bmatrix} + \sum_{n=k}^M \begin{bmatrix} x_{dn}(m) \\ y_{dn}(m) \end{bmatrix} \quad (20)$$

where  $x_a(m)$  and  $y_a(m)$  are the approximated residual signals, and  $x_{dn}(m)$  and  $y_{dn}(m)$  are the detailed signals corresponding to the  $m$ th point of the sequence. The approximated signals in terms of scaling functions  $\phi_{mk}$  is gives as [23, 24]

$$\begin{aligned} x_a(m) &= \sum_k a_k \phi_{Mk}(m) \\ y_a(m) &= \sum_k c_k \phi_{Mk}(m) \end{aligned} \quad (21)$$

where subscript  $M$  means the maximum level of decomposition, and  $k$  is the translation index. The detailed signals in terms of wavelet functions  $\psi_{ml}$  are given as [21, 22]

$$\begin{aligned} x_{dn}(m) &= \sum_n r_{pn} \psi_{pn}(m) \\ y_{dn}(m) &= \sum_n d_{pn} \psi_{pn}(m) \end{aligned} \quad (22)$$

where subscripts  $p = 1, 2, \dots, M$  mean the succeeding levels of decomposition. The wavelet descriptors are created here by coefficients  $a_n, c_n$ , representing the approximated signal and by the set of  $r_{pn}d_{pn}$  ( $p = 1, 2, \dots, M$ ), representing the detailed signals of  $M$  applied levels of decomposition.

The complete WT features are arranged into one-dimensional vector. These features are further normalised, making them independent of the scale and orientation [24]. As a result of such normalization, we get wavelet descriptors invariant to the scale and rotation. Further, to make the feature vector compact, the first 100 coefficients are selected from the rest of the descriptor without losing relevant information of the target. This feature provides the identity to shape of the target. With the use of these descriptors, the target can be discriminated. After feature vectors are obtained, these feature vectors will be fed to ANN for training. Although many classifiers are available in the literature, neural network is very promising over other classifiers. Further, to increase the detection accuracy of the ANN model, a lot of training data are required. Therefore to increase data, synthetic data of three common shapes of various sizes and orientations of target are generated using Boolean values as given in Appendix A [18, 19]. The synthetic target shape has been obtained based on a priori information of target size, location, and size of pixel [20]. For example, synthetic data of rectangular shape of sizes  $(50 \times 30)$ ,  $(45 \times 25)$  cm,  $(55 \times 35)$  cm,  $(60 \times 40)$  cm, and  $(65 \times 45)$  at orientations 0, 30, 60, 90, 120, 150, and 180 degrees have been generated. Similarly, synthetic data of square shape of sizes  $(30 \times 30)$ ,  $(35 \times 35)$  cm  $(40 \times 40)$  cm,  $(45 \times 45)$  cm, and  $(50 \times 50)$  cm at orientations 0, 30, 60, 90, 120, 150, and 180 degrees have been generated, and synthetic data of circle shape of sizes  $(30 \times 30)$ ,  $(35 \times 35)$  cm  $(40 \times 40)$  cm,  $(45 \times 45)$  cm, and  $(50 \times 50)$  cm at orientation 0 have been generated. The number of target pixels in the synthetic image is obtained based on a priori information of target size, location, and size of pixel [16]. Figures 5(a), (b) & (c) show synthetic image of circular, square, and rectangular shapes of sizes 30 cm  $\times$  30 cm, 30 cm  $\times$  30 cm, and 50 cm  $\times$  30 cm. In Figure 5, X-axis represents the height, and Y-axis represents the horizontal cross-range. On X and Y axes, pixel points are shown having 1 unit = 0.5 cm.

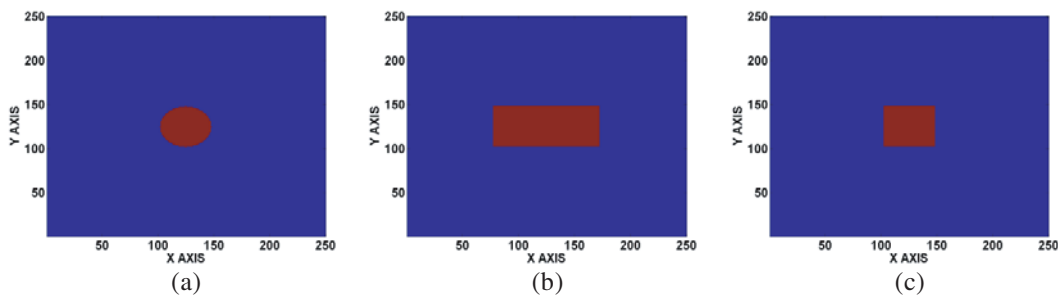


**Figure 5.** (a) Synthetic image of the circular shape of size 30 cm. (b) Synthetic image of the rectangle shape of size 50 cm  $\times$  30 cm. (c) Synthetic image of the square shape of size 30 cm  $\times$  30 cm.

Thus, a total of 75 synthetic samples S1-S75 of data have been used to train the neural network. From these synthetic data, the feature is extracted. After obtaining all the features of the particular shape of a target for example circular, it is arranged in the form of a column vector. Similarly, features for square shape and rectangular shape have been obtained and arranged in the form of a column vector. A simple feed-forward network with one hidden layer and one output layer with backprojection training algorithm is used to train the network [25]. Among the 75 samples, we have randomly selected 70% of samples for training and the remaining 30% for validation, and testing point of view in ratios of 15% and 15%, respectively. The desired neural network configuration setup is shown in Figure 6. The number of neurons in input layer is equal to feature vector dimension. The hidden layer consists of 50 neurons. The numbers of neurons are chosen on the basis of trial and error in order to maintain the balance between ANN system complexity as well as minimizing the output error. The output layer consists of 3 neurons. The teaching pattern for circular shape object is  $(1, 0, 0)$ , for square shape object is  $(0, 1, 0)$ , and for rectangular shape object is  $(0, 0, 1)$ . Sigmoid transfer function is chosen for the hidden and output layer so that output of a neural network lies between 0 and 1 which is required for image reconstruction. Mean squared error (MSE) criterion is used as learning algorithm to train the

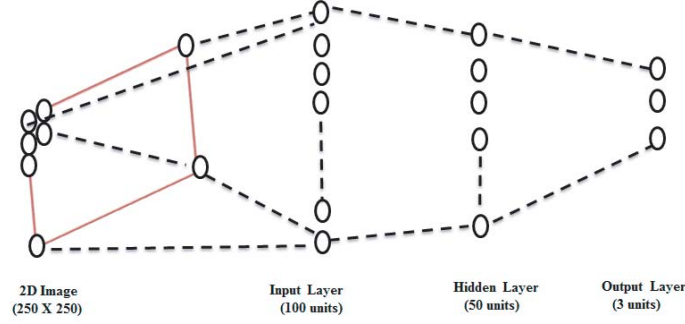


**Figure 6.** Neural network configuration for shape identification.

neural network which is defined as

$$mse = \frac{1}{N} \sum_{i=1}^N e_i^2 = \frac{1}{N} \sum_{i=1}^N (r_i - a_i)^2 \quad (23)$$

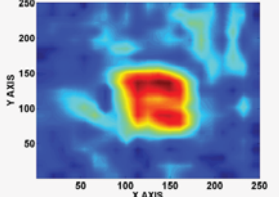
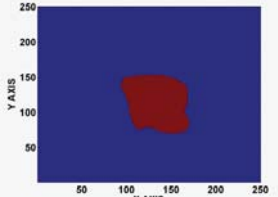
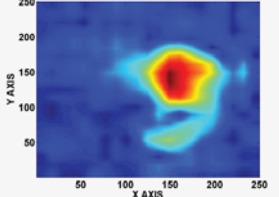
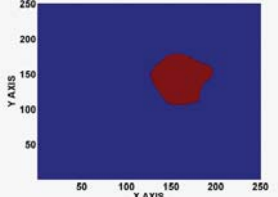
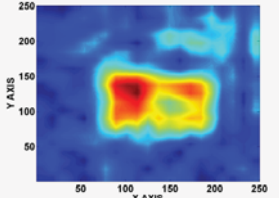
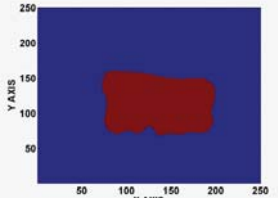
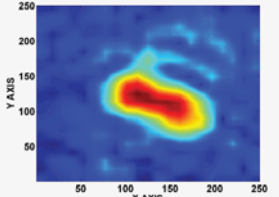
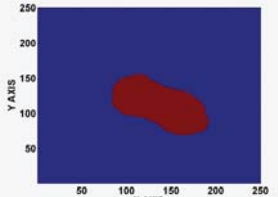
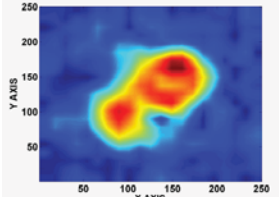
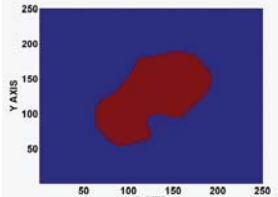
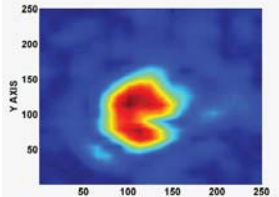
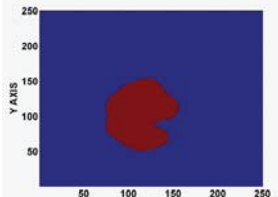
where ‘ $a$ ’ is the network outputs, and ‘ $r$ ’ is the target outputs. In MSE criteria the neural network first produces its own output vector ‘ $a$ ’ according to fed input vector and then compares the output vector with the desired target vector ‘ $t$ ’. If an error occurs, then the weights are adjusted using the scaled conjugate gradient method to reduce the difference until MSE reaches below 0.01 for optimum performance. The performance of the neural network is better for the lower value of mean square error.

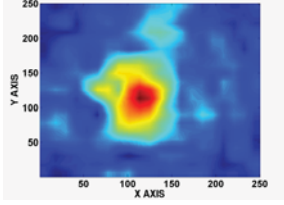
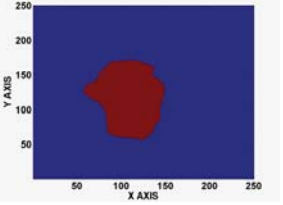
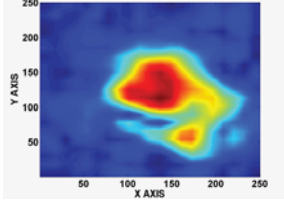
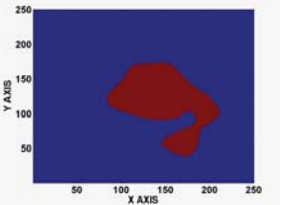
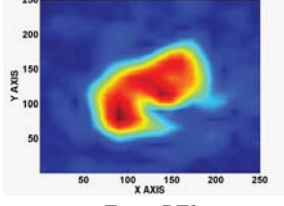
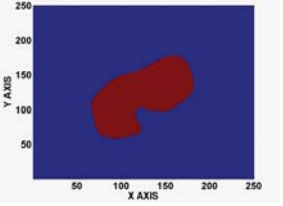
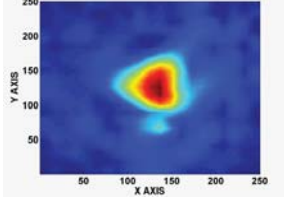
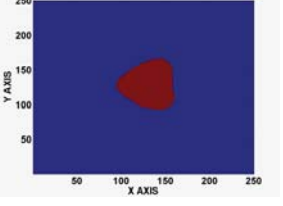
**Table 6.** List of real independent target samples used for testing of neural network.

Target ID	Shape	Size (Length $\times$ Width)	Orientation	Material
RT1	Square	30 cm $\times$ 30 cm	0	Wood
RT2	Square	35 cm $\times$ 35 cm	135	Wood
RT3	Rectangle	50 cm $\times$ 30 cm	0	Wood
RT4	Rectangle	50 cm $\times$ 30 cm	45	Wood
RT5	Rectangle	55 cm $\times$ 35 cm	135	Wood
RT6	Square	30 cm $\times$ 30 cm	45	Metal
RT7	Square	35 cm $\times$ 35 cm	0	Metal
RT8	Rectangle	50 cm $\times$ 30 cm	45	Metal
RT9	Rectangle	55 cm $\times$ 35 cm	135	Metal
RT10	Circle	Dia = 35 cm	0	Metal

After training, the performance of a trained artificial neural network needs to be verified through independent data to confirm its usefulness and practicality. For this purpose, ten independent test samples RT1, RT2, RT3, RT4, RT5, RT6, RT7, RT8, RT9, and RT10 of different shapes and sizes of targets are experimentally generated by real scanning of target. These test samples have not been used earlier for training in any form. The details of the targets are given in Table 6. The raw 2D TWRI images of test samples T2, T5, T6, T7, T8, T9, T10, T11, T12, and T13 are shown in Table 7. The test samples are thresholded using Eq. (13) as shown in Table 7, and then features are extracted using the wavelet transform from the boundary of their target. These features are input to the trained neural network to get the output. Table 7 shows the outcomes of the developed ANN models for different independent target samples. It can be observed that with these test samples, the trained neural network shows fairly good performance. The experimental result shows that the retrieved result of shape is in good agreement with original shape. Thus, the experimental results confirm the capability of the proposed orientation and scale-invariant neural network for shape recognition of the considered three regular target shapes. Further, the proposed neural network methodology can also be checked on

**Table 7.** Results of developed ANN model with independent test data sample.

Real Test Sample	Thresholded image	Shape Identified using ANN	Actual Shape
 <p data-bbox="461 604 558 632">Target RT1</p>		Square	Square
 <p data-bbox="461 863 558 890">Target RT2</p>		Square	Square
 <p data-bbox="461 1121 558 1148">Target RT3</p>		Rectangle	Rectangle
 <p data-bbox="461 1379 558 1407">Target RT4</p>		Rectangle	Rectangle
 <p data-bbox="461 1638 558 1665">Target RT5</p>		Rectangle	Rectangle
 <p data-bbox="461 1896 558 1923">Target RT6</p>		Square	Square

 <p>Target RT7</p>		Square	Square
 <p>Target RT8</p>		Rectangle	Rectangle
 <p>Target RT9</p>		Rectangle	Rectangle
 <p>Target RT10</p>		Circle	Circle

different irregular target shapes. As a future work plan, more sophisticated and practical target shapes will be considered for shape recognition.

#### 4. CONCLUSION

In this paper, our main focus is to first critically analyze different imaging algorithms on real data to select an effective imaging algorithm. Different imaging techniques have been applied to TWI data, and a comparison of obtained images is carried out. As per our experimental observations with various target samples, a considerable difference between the output images of algorithms from the focusing point of view is found. Though the considered imaging algorithm can accurately locate the position of the target, BP and F-K algorithms perform poorly in detecting target sizes and shapes compared to delay and sum beamforming imaging algorithms. It is observed that peak to signal noise ratio of formed images using the delay and sum beamforming imaging technique is high compared to backprojection and frequency-wavenumber imaging algorithms. It is also observed that delay and sum imaging algorithm can be effectively used to detect approximate shape and size of the target with low false alarm as compared to frequency-wavenumber and backprojection. However, the processing time required for the delay and sum algorithm is high as compared to the frequency-wavenumber algorithm. Further, a wavelet descriptor based ANN model has been developed for shape recognition of target from the through-the-wall images formed using delay and sum beamforming. The experimental results show that the developed ANN model has correctly recognized the shape of real target samples irrespective to the orientation of the target.

## APPENDIX A.

Table A1. List of samples used for training of neural network.

Target ID	Shape	Size (length $\times$ width)	Orientation	Generated Image
S1	Circle	Dia = 30 cm	0	Synthetic
S2	Circle	Dia = 35 cm	0	Synthetic
S3	Circle	Dia = 40 cm	0	Synthetic
S4	Circle	Dia = 45 cm	0	Synthetic
S5	Circle	Dia = 50 cm	0	Synthetic
S6	Rectangle	45 cm $\times$ 25 cm	0	Synthetic
S7	Rectangle	45 cm $\times$ 25 cm	30	Synthetic
S8	Rectangle	45 cm $\times$ 25 cm	60	Synthetic
S9	Rectangle	45 cm $\times$ 25 cm	90	Synthetic
S10	Rectangle	45 cm $\times$ 25 cm	120	Synthetic
S11	Rectangle	45 cm $\times$ 25 cm	150	Synthetic
S12	Rectangle	50 cm $\times$ 30 cm	0	Synthetic
S13	Rectangle	50 cm $\times$ 30 cm	30	Synthetic
S14	Rectangle	50 cm $\times$ 30 cm	60	Synthetic
S15	Rectangle	50 cm $\times$ 30 cm	90	Synthetic
S16	Rectangle	50 cm $\times$ 30 cm	120	Synthetic
S17	Rectangle	50 cm $\times$ 30 cm	150	Synthetic
S18	Rectangle	55 cm $\times$ 35 cm	0	Synthetic
S19	Rectangle	55 cm $\times$ 35 cm	30	Synthetic
S20	Rectangle	55 cm $\times$ 35 cm	60	Synthetic
S21	Rectangle	55 cm $\times$ 35 cm	90	Synthetic
S22	Rectangle	55 cm $\times$ 35 cm	120	Synthetic
S23	Rectangle	55 cm $\times$ 35 cm	150	Synthetic
S24	Rectangle	60 cm $\times$ 40 cm	0	Synthetic
S25	Rectangle	60 cm $\times$ 40 cm	30	Synthetic
S26	Rectangle	60 cm $\times$ 40 cm	60	Synthetic
S27	Rectangle	60 cm $\times$ 40 cm	90	Synthetic
S28	Rectangle	60 cm $\times$ 40 cm	120	Synthetic
S29	Rectangle	60 cm $\times$ 40 cm	150	Synthetic
S30	Rectangle	65 cm $\times$ 45 cm	0	Synthetic
S41	Rectangle	65 cm $\times$ 45 cm	30	Synthetic
S42	Rectangle	65 cm $\times$ 45 cm	60	Synthetic
S43	Rectangle	65 cm $\times$ 45 cm	90	Synthetic
S44	Rectangle	65 cm $\times$ 45 cm	120	Synthetic
S45	Rectangle	65 cm $\times$ 45 cm	150	Synthetic
S46	Square	30 cm $\times$ 30 cm	0	Synthetic
S47	Square	30 cm $\times$ 30 cm	30	Synthetic
S48	Square	30 cm $\times$ 30 cm	60	Synthetic
S49	Square	30 cm $\times$ 30 cm	90	Synthetic

S50	Square	30 cm × 30 cm	120	Synthetic
S51	Square	30 cm × 30 cm	150	Synthetic
S52	Square	35 cm × 35 cm	0	Synthetic
S53	Square	35 cm × 35 cm	30	Synthetic
S54	Square	35 cm × 35 cm	60	Synthetic
S55	Square	35 cm × 35 cm	90	Synthetic
S56	Square	35 cm × 35 cm	120	Synthetic
S57	Square	35 cm × 35 cm	150	Synthetic
S58	Square	40 cm × 40 cm	0	Synthetic
S59	Square	40 cm × 40 cm	30	Synthetic
S60	Square	40 cm × 40 cm	60	Synthetic
S61	Square	40 cm × 40 cm	90	Synthetic
S62	Square	40 cm × 40 cm	120	Synthetic
S63	Square	40 cm × 40 cm	150	Synthetic
S64	Square	45 cm × 45 cm	0	Synthetic
S65	Square	45 cm × 45 cm	30	Synthetic
S66	Square	45 cm × 45 cm	60	Synthetic
S67	Square	45 cm × 45 cm	90	Synthetic
S68	Square	45 cm × 45 cm	120	Synthetic
S69	Square	45 cm × 45 cm	150	Synthetic
S70	Square	50 cm × 50 cm	0	Synthetic
S71	Square	50 cm × 50 cm	30	Synthetic
S72	Square	50 cm × 50 cm	60	Synthetic
S73	Square	50 cm × 50 cm	90	Synthetic
S74	Square	50 cm × 50 cm	120	Synthetic
S75	Square	50 cm × 50 cm	150	Synthetic

## REFERENCES

1. Baranoski, E. J., “Through-wall imaging: Historical perspective and future directions,” *Journal of the Franklin Institute*, Vol. 345, 556–569, 2008.
2. Smith, G. E. and B. G. Mobasser, “Robust through-the-wall radar image classification using a target-model alignment procedure,” *IEEE Transactions on Image Processing*, Vol. 21, 754–767, 2011.
3. Hantscher, S., B. Praher, A. Reiszahn, and C. G. Diskus, “Comparison of UWB target identification algorithms for through-wall imaging applications,” *IEEE European Radar Conference*, 104–107, 2006.
4. Kidera, S., T. Sakamoto, and T. Sato, “High-resolution 3-D imaging algorithm with an envelope of modified spheres for UWB through-the-wall radars,” *IEEE Transactions on Antennas and Propagation*, Vol. 57, 3520–3529, 2009.
5. Dogaru, T. and C. Le, *Through-the-wall Small Weapon Detection Based on Polarimetric Radar Techniques*, Army Research Lab Adelphi MD Sensors and Electronic Devices Directorate, No. ARL-TR-5041, 2009.
6. Mirbach, M. and W. Menzel, “A simple surface estimation algorithm for UWB pulse radars based on trilateration,” *IEEE International Conference on Ultra-Wideband (ICUWB)*, 273–277, 2011.

7. Wu, S., Y. Xu, J. Chen, S. Meng, G. Fang, and H. Yin, "Through-wall shape estimation based on UWB-SP radar," *IEEE Geoscience and Remote Sensing Letters*, Vol. 10, 1234–1238, 2013.
8. Dehmollaian, M., "Through-wall shape reconstruction and wall parameters estimation using differential evolution," *IEEE Geoscience and Remote Sensing Letters*, Vol. 8, 201–205, 2010.
9. Ahmad, F., M. G. Amin, and S. A. Kassam, "Synthetic aperture beamformer for imaging through a dielectric wall," *IEEE Transactions on Aerospace and Electronic Systems*, Vol. 41, 271–283, 2005.
10. Hunt, A. R., "Use of a frequency-hopping radar for imaging and motion detection through walls," *IEEE Transactions on Geoscience and Remote Sensing*, Vol. 47, 1402–1408, 2009.
11. Ahmad, F., Y. Zhang, and M. G. Amin, "Three-dimensional wideband beamforming for imaging through a single wall," *IEEE Geoscience and Remote Sensing Letters*, Vol. 5, 176–179, 2008.
12. Hantscher, S., B. Praher, A. Reiszahn, and C. G. Diskus, "Analysis of imaging radar algorithms for the identification of targets by their surface shape," *Int. Conf. on UWB*, 2006.
13. Yigit, E., S. Demirci, C. Ozdemir, and A. Kavak, "A synthetic aperture radar-based focusing algorithm for B-scan ground penetrating radar imagery," *Microwave and Optical Technology Letters*, Vol. 49, 2534–2540, 2007.
14. Ozdemir, C., S. Demirci, and E. Yigit, "Practical algorithms to focus B-scan GPR images: Theory and application to real data," *Progress In Electromagnetics Research B*, Vol. 6, 109–122, 2008.
15. Verma, P. K., A. N. Gaikwad, D. Singh, and M. J. Nigam, "Analysis of clutter reduction techniques for through wall imaging in UWB range," *Progress In Electromagnetics Research B*, Vol. 17, 29–48, 2009.
16. Muqaibel, A. H. and A. Safaai-Jazi, "A new formulation for characterization of materials based on measured insertion transfer function," *IEEE Transactions on Microwave Theory and Techniques*, Vol. 51, 1946–1951, 2003.
17. Chandra, R., A. N. Gaikwad, D. Singh, and M. J. Nigam, "An approach to remove the clutter and detect the target for ultra-wideband through-wall imaging," *Journal of Geophysics and Engineering*, Vol. 5, 412–419, 2008.
18. Singh, D., N. K. Choudhary, K. C. Tiwari, and R. Prasad, "Shape recognition of shallow buried metallic objects at X-band using ANN and image analysis techniques," *Progress In Electromagnetics Research B*, Vol. 13, 257–273, 2009.
19. Ibrahim, K. M., K. F. A. Hussein, and A.-E.-H. A.-E.-A. Ammar, "Land-buried object detection and target-shape recognition in lossy and dispersive soil," *Progress In Electromagnetics Research B*, Vol. 57, 279–298, 2014.
20. Kumar, B., R. Upadhyay, and D. Singh, "Development of an adaptive approach for identification of targets (match box, pocket diary and cigarette box) under the cloth with MMW imaging system," *Progress In Electromagnetics Research B*, Vol. 77, 37–55, 2017.
21. "Easyfit by mathwave technologies," [Online]. Available:<http://www.mathwave.com/easyfit-distribution-fitting.html>.
22. Forbes, C., E. Merran, H. Nicholus, and P. Brian, *Statistical Distributions*, John Wiley and Sons, New Jersey, 2011.
23. Gonzalez, S. and W. Richards, *Digital Image Processing*, Dorling Kindersley, New Delhi, 2009.
24. Osowski, S., "Fourier and wavelet descriptors for shape recognition using neural networks — A comparative study," *Pattern Recognition*, Vol. 35, 1949–1957, 2002.
25. Haykin, S., *Neural Network a Comprehensive Foundation*, Pearson Education, New Delhi, 2005.